J Seismol (2012) 16:797–814
DOI 10.1007/s10950-011-9255-6

ORIGINAL ARTICLE

Rotation of vertically oriented objects during earthquakes

Klaus-G. Hinzen

Received: 7 July 2011 / Accepted: 20 October 2011 / Published online: 19 November 2011

Abstract Vertically oriented objects, such as tombstones, monuments, columns, and stone lanterns, are often observed to shift and rotate during earthquake ground motion. Such observations are usually limited to the mesoseismal zone. Whether near-field rotational ground motion components are necessary in addition to pure translational movements to explain the observed rotations is an open question. We summarize rotation data from seven earthquakes between 1925 and 2009 and perform analog and numeric rotation testing with vertically oriented objects. The free-rocking motion of a marble block on a sliding table is disturbed by a pulse in the direction orthogonal to the rocking motion. When the impulse is sufficiently strong and occurs at the 'right' moment, it induces significant rotation of the block. Numeric experiments of a free-rocking block show that the initiation of vertical block rotation by a cycloidal acceleration pulse applied orthogonal to the rocking axis depends on the amplitude of the pulse and its phase relation to the rocking cycle. Rotation occurs when the pulse acceleration exceeds the threshold necessary to provoke rocking of a resting block, and the rocking block approaches its equilibrium position. Experiments with blocks subjected to full 3D strong motion signals measured during the 2009 L'Aquila earthquake confirm the observations from the tests with analytic ground motions. Significant differences in the rotational behavior of a monolithic block and two stacked blocks exist.

Keywords Earthquake · Numeric model · Translational ground motion · Rotation · Vertically oriented object · Cycloidal pulse

K.-G. Hinzen (✉)
Earthquake Geology and Archaeoseismology Group,
Cologne University,
Vinzenz-Pallotti-Str. 26,
51429 Bergisch Gladbach, Germany
e-mail: hinzen@uni-koeln.de

1 Earthquake rotated objects

Earthquake rotated objects (EROs, Fig. 1) have been described in the literature for over a century. The pure description of rotated objects was followed by the first attempts to explain the driving mechanism of EROs by Hoffmann (1838) and Mallet (1862). With the advent of instrumental seismology, interest in these specific macroseismic effects was not as strong as in the late nineteenth century. Those early efforts concentrated on back-calculate ground motion parameters from toppled and rotated objects (Mallet 1848, 1862). Mallet (1848) proposed an uneven distribution of contact forces with respect to the center of gravity of a vertically oriented object as a possible cause of rotation. Kozák (2006) calls this the Rot1 hypothesis while he assigned Rot2 to rotation due to the combination of vibrations at right angles as hypothesized by Hoffmann (1838), Mallet (1862), and Reid (1910). Kozák (2009) gave a review of historical examples of EROs.

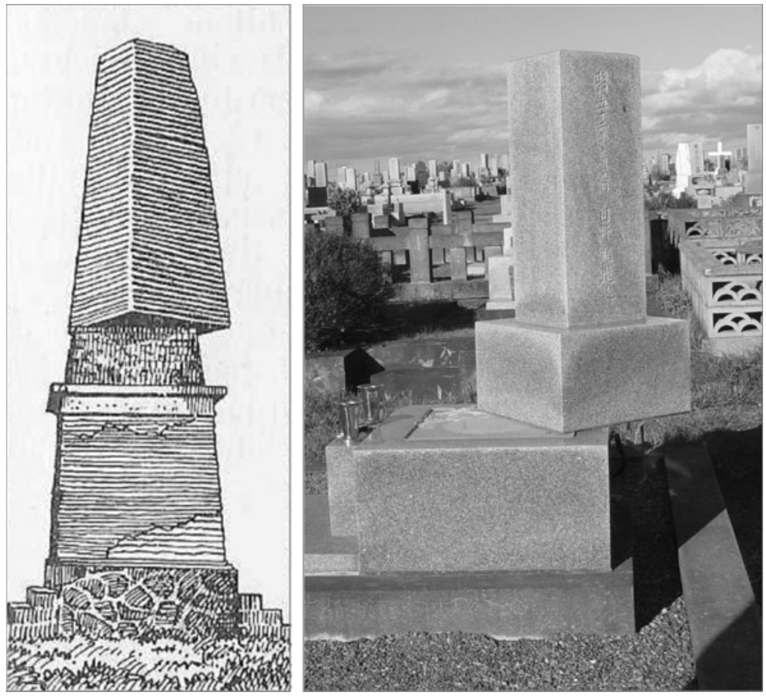

Fig. 1 Old and recent examples of earthquake rotated objects. *Left* obelisk erected in 1850 at Chatak, India, which broke and rotated counter-clockwise during the 1897 Assam earthquake; documented by Oldham (1899). *Right* dislocated and ccw rotated tombstones in the Kushiro Cemetery after the Tokachi-Oki Earthquake, 2003-09-26 (photo courtesy of R. Anooshepoor)

Rotated and toppled monuments, tombstones, and other vertically oriented objects are a common observation in populated epicentral areas and observations of such effects became part of most macroseismic intensity scales. Sieberg (1923) revised the Mercalli-Cancani intensity scale (Cancani 1903) and associated EROs with intensity grade VII destructive (*zerstörend*): "Statues, Tombstones and similar objects, near the ground, also those in churches, graveyards, public parks, etc., rotate on their pedestals or fall." He linked grade VIII to accelerations between 0.25 and 0.5 m/s^2. The modified Mercalli scale (MM) (Wood and Neumann 1931) in its 1956 version (Richter 1958) grades EROs with degree VII: "Twisting, fall of chimneys, factory stacks, monuments, towers, elevated tanks." The EMS scale (Grünthal 1993) grades rotations higher: grade VIII (heavily damaging) includes: "Tombstones may be occasionally displaced, twisted or overturned," and a criteria for grade IX (destructive) is: "Many monuments and columns fall or are twisted."

With the advent of increasingly sophisticated seismometers to measure translational ground motion during an earthquake, macroseismic observations were no longer needed to fix the coordinates of the event, and less attention was paid to EROs. Comments by Gutenberg (1927) and also Richter (1958) in their seminal textbooks supported the hypothesis that rotation is not especially significant in earthquake seismology as referenced by Cucci and Tertulliani (2011). However, as shown in Fig. 2, some surveys of EROs have been made also during the instrumental period of seismology.

Figure 2 summarizes macroseismic survey data including locations and sense of rotation in polar plots centered at the epicenter. Hodgson (1950) studied EROs caused by the February 28 1925 St. Lawrence earthquake in Quebec (Fig. 2) which following Kovach (2004) had a moment magnitude of 6.8 and a thrust mechanism on a northeast–southwest striking and 45° dipping fault plane. Hodgson (1950) reports a tendency of clockwise (cw) rotations north of the St. Lawrence River and counter-clockwise (ccw) to the south; however, he points out the scarcity of data in the north and concludes that rotations do not provide any reliable indication of the source location other than a general one; namely, rotations occur close to the epicenter. Photos of several EROs are available at the website of St. Louis University, Earth and Atmospheric Sciences (Whittington and Pascek 2005).

Ulrich (1936) summarized the earthquake activity in Helene, Montana. After the earthquake of October 31 in 1935 with maximum intensity VI–VII, observers reported that, in general, chimneys, stacks, and tombstones moved in a ccw direction in or near Helena and

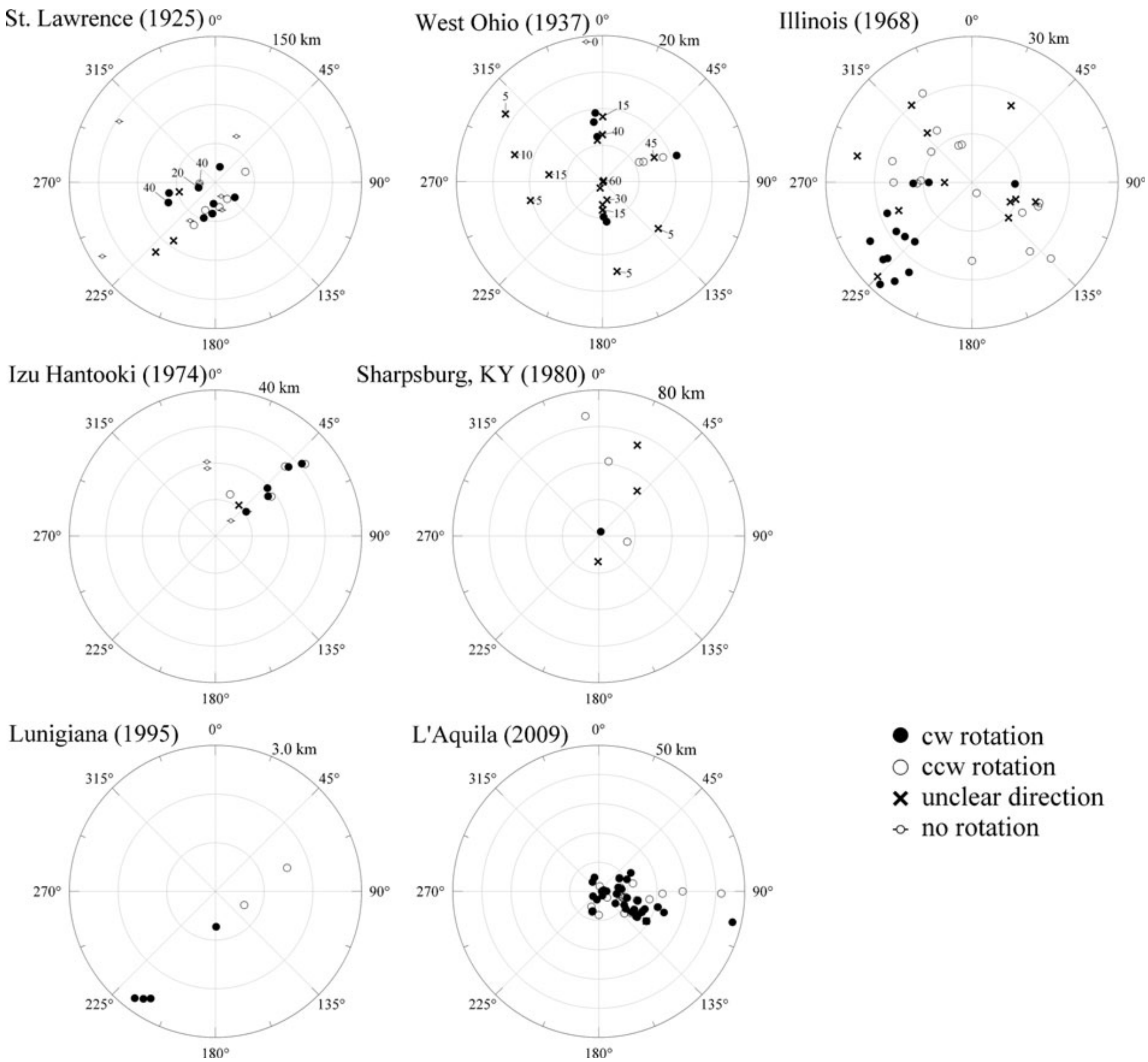

Fig. 2 Polar plots of the distribution of the rotation of EROs in seven earthquakes. *Open and filled circles* in the polar plot indicate clockwise and counter-clockwise rotation of EROs; *crosses* indicate that the direction of rotation was ambiguous, and *small circles* indicate that no movement occurred, if available rotation angle in degree is shown by the labels. The angle corresponds to the azimuth and the radial axis to the epicentral distance. The scale values for the latter are indicated at the outer circle in the NNE. The data are taken from Hodgson (1950), Rouse and Priddy (1938), Gordon et al. (1970), Yamaguchi and Odaka (1974), Mauk et al. (1982), Tertulliani and Maramai (1998), and Cucci and Tertulliani (2011)

that several miles north of Helena, the rotation was in a cw direction.

Rouse and Priddy (1938) present observations which were made during two earthquakes in Western Ohio on March 2 and 9, 1937. These earthquakes were felt in Ohio and Kentucky, Indiana, Michigan, western Pennsylvania, and West Virginia. After each earthquake, a survey of western Ohio was made of property damage, movement of objects in buildings, displacement of monuments in cemeteries, and numerous other phenomena. Rouse and Priddy (1938) combined the results from both earthquakes (Fig. 2) because they claim that the two earthquakes had the same epicenter. Rotations were observed at distances up to 20 km from the epicenter mostly on vertically oriented gravestones in cemeteries.

Lander (1968) reported an interesting observation of rotated tombstones during the April 25 North California earthquake, with a maximum intensity of MM VII. In the graveyard of Santa Rosa, no gravestones were toppled, but a number of columnar pedestals were rotated. In the northern and central part of the cemetery, about 20 pedestals were rotated 2.5 cm in a cw sense relative to their bases (Lander 1968), and none rotated ccw. At the southern end of the cemetery, eight pedestals were rotated in a ccw sense by about the same amount.

Gordon et al. (1970) made a detailed documentation of EROs during the November 9, 1968 m_b 5.3 South-Central Illinois earthquake. Of the more than 40 single observations, roughly one third showed clear cw and one third ccw rotations, while for the rest, the direction of rotation was ambiguous or exhibited no movement (Fig. 2). They found a clear concentration of ccw rotations in the southwestern quadrant with respect to the epicenter while north and south east of the epicenter mainly cw rotation occurred. No observations were available from the northeastern quadrant. Their study strongly suggests a correlation of the radiation pattern of the earthquake source and the sense of rotation. This is a remarkable observation as the objects were of different kinds and sizes listing among others tombstones, chimneys, and heavy furniture.

Yamaguchi and Odaka (1974) did a field study of the May 9, 1974 Izu-Hantooki earthquake and correlated rotation and toppling directions of gravestones and stone lanterns with the polarization direction of S-waves. Mauk et al. (1982) documented movement of EROs during the July 27, 1980 Sharpburg Kentucky earthquake (Fig. 2). This magnitude 5.1 event was widely felt in the Eastern United States and had intensity VII in the epicentral area. Mechanism was a right lateral strike slip with a small thrust component (Mauk et al. 1982). The strong Spitak earthquake in 1988 caused widespread damage in Armenia. Yegian et al. (1994) reported numerous rotations of tombstones in cemeteries in Spitak and Leninakan. They used toppling and rotation information to deduce the possible range of PGA values for those locations, supporting their conclusions by comparisons with scaled shake table tests.

Tertulliani and Maramai (1998) provided data about EROs from the ML 4.8 earthquake of October 10, 1995 in the Lunigiana region in northwestern Italy (Fig. 2). Though this was light earthquake, rotation of vertically oriented objects seemed coherent with the earthquake's source mechanism. The plot of these effects on the epicentral map shows two well-clustered groups of rotations, respectively, clockwise and counter-clockwise. Tertulliani and Maramai (1998) mentioned that these clusters might be related to s-wave radiation of the focal mechanism proposed by Frepoli and Amato (1997). They suggested the use of EROs in order to constrain the source mechanism of historical events.

The most comprehensive recent study of EROs was made by Cucci and Tertulliani (2011) from the L'Aquila, 2009 earthquake in Italy. They compiled a dataset of 105 EROs from the epicentral zone of the M_W 6.3 event. The distribution of EROs suggests correspondence with source directivity, with the EROs mainly found southeast of the epicenter (Fig. 2). The site effects mainly attributable to near-surface geological conditions, revealed a clear correlation between ground amplification and the frequency of occurrence of EROs. However, the sense of rotation is distributed randomly and a question is how much influence comes from the ground motion and how much the sense of rotation is determined by the EROs structure, placement, and subsoil conditions. The large differences of distances up to which EROs are reported, 3 km for the ML 4.8 Lunigiana earthquake in 1995 and more than 60 km for the magnitude 5.1 Sharpburg Kentucky earthquake in 1980, is not only a question of magnitude. Source depth, directivity, and site effects are obviously also crucial effects.

The observations summarized in Fig. 2 indicate some patterns of the sense of rotation of EROs. However, it should be noticed that tombstones within one graveyard are often of similar size and structure. This could be an explanation for similar rotation of several objects within a small area, especially where there is also minor variation of the ground motion. Different degrees of slenderness of objects will inevitably lead to a different rotational behavior according to the Rot2 mechanism (Kozák 2006).

The recent lively discussions on rotational ground motion components, especially those in the source region of earthquakes, included discussions of EROs (i.e., Yang et al. 2010: Hinzen 2010; Cucci and Tertulliani 2011, Grazier and Kalkan 2012). New instruments are being developed which can directly measure rotational components of ground motion (i.e., Nigbor et al. 2009; Schreiber et al. 2009b; Takamori et al. 2009, Brokesova et al. 2012; Bernauer et al. 2012). While the measurement of rotational motion in the teleseismic wavefield made large advances with the advent of ringlaser instruments (Schreiber et al. 2009a), the measurement of rotations in the near field of the earthquake source are still a challenge (Cowsik et al. 2009). Rotations evaluation in the near field could be important to learn more about source mechanisms and in particular to assess the role of this component of motion in seismic engineering and, thus, its potential in causing EROs (Trifunac 2009; Stupazzini et al. 2009). The references from which the examples of ERO observations in Fig. 2 were taken show that these can be successfully used to estimate ground acceleration levels and eventually constrain source mechanisms of historic earthquakes. However, some examples show rather random distribution of cw and ccw rotations. Here the question is of how much influence comes from the ground motion and how much the sense of rotation is determined by the EROs structure, placement, and subsoil conditions.

In this paper we address the question of whether vertically oriented objects can suffer rotations during an earthquake when pure translational ground motions are taken into account, and if so, what conditions generate such movements. We use very basic analog experiments with a vertically oriented marble block and numeric models of one and two stacked discrete elements to test Kozák's Rot2 mechanism. We start with simple tests where rocking vertically oriented objects experience ground motion in a direction orthogonal to the rocking motion. This can be seen as an analogue to S-waves followed by later arrivals of scattered or reflected phases, waves with different polarizations from sections of a complex rupture process, or the onset of surface waves.

2 Analog experiments

A simple sliding table and a marble block of 6×8×30 cm (Fig. 3) were used in a series of manual experiments which were performed to test the behavior of a rocking rectangular block when a motion perpendicular to the rocking direction is applied. With a mass of 4,267 g, the block has a density of 2.96 Mgm^{-3}. Figure 3 describes the experiment. The table plate (16×19 cm) is made of aluminum. Four linear roll bearings and two round guide bars of 20 mm diameter allow only a single component of motion for the table. Four accelerometers were used to measure the block and table motion during the experiments. A small (18×18×3 mm) three-component accelerometer with a weight of 1.2 g was attached to the top of the marble block and oriented parallel to the block edges (Fig. 3). In addition, a one-component accelerometer was fixed to the sliding table parallel to its one degree of freedom. Data were acquired with a four-channel 24 Bit AD converter at a sampling rate of 1 kHz. The accelerometers were calibrated by turning them 90° and 180° with respect to the direction of gravity corresponding to 1.0 and 2.0 g steps in the acceleration records. This experiment with a "perfect" flat table plate is strong idealization of the conditions of real EROs as those for example shown in Fig. 1.

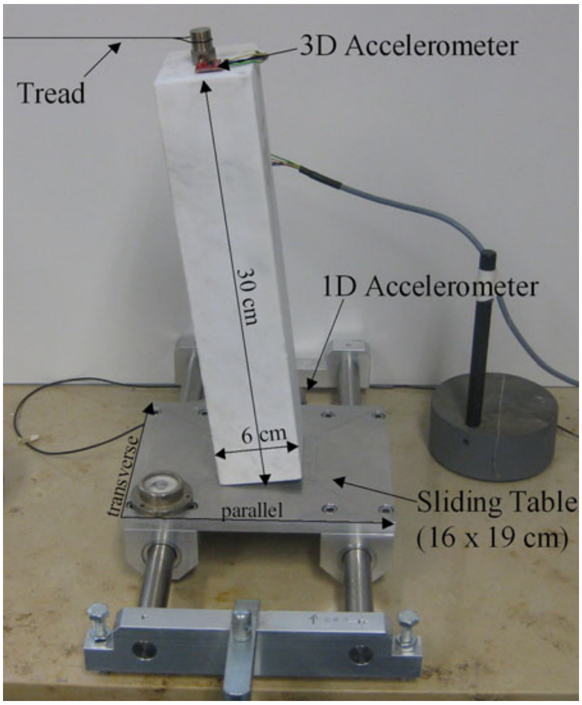

Fig. 3 Description of the analog experiment with a vertically oriented marble block on a sliding table. The block was inclined to an angle close to the turning point by a thin thread, which was released to initiate a rocking motion in the direction labeled parallel. Short "hand-driven" impulses were applied to the sliding table in the transverse direction. A 3D accelerometer on top of the block and a 1D accelerometer at the sliding table were used to control the blocks movement

Two free-rocking block tests were made with the rocking edges along the long and short side of the base, respectively, and a fixed sliding table. The friction between block and base was large enough to prevent sliding of the block. Figure 4 defines all model parameters and shows the restoring gravity moment M as a function of the rotation angle θ (Augusti and Sinopoli 1992). The rocking motion of such a freestanding rectangular block has been extensively discussed in the literature (e.g., Kirkpatrick 1927; Housner 1963; Shi et al. 1996; Anooshehpoor et al. 1999; Makris and Roussos 2000; Zhang and Makris 2000; Anooshehpoor et al. 2000; Zhang and Makris 2001; Hinzen 2011). The block has height $2h$ and width $2b$; the half-diagonal $R = \sqrt{h^2 + b^2}$, is defined as the distance from the center of gravity, cg to the actual center of rotation of the block, A and A', respectively. The angle between the longer block side, which coincides with vertical direction when the block is at rest, and the line R is α and the inclination (rotation) of the block, is θ. Housner (1963) solved the equations of motion for the rocking block for one degree of freedom, i.e., the rotation about the corner points A and A'. This movement constraint specifies that (1) the friction at the corner points is large enough that no sliding between the block and the base occurs and (2) the block does not bounce during the movement through the static equilibrium. The equation of motion of the free-rocking response of a 2D rigid block without sliding, slide-rocking or free flight behavior was given by Housner (1963):

$$I_0 \ddot{\theta} = -WR \sin(\alpha - \theta) \tag{1}$$

in which $I_0 = 4/3 \cdot mR^2$ is the mass moment of inertia of a homogeneous rectangular block about corner A and $W{=}mg$ is the weight of the homogenous block, m and g are the block mass and acceleration of gravity, respectively. For slender blocks ($\sin\alpha \approx \alpha$) Eq. 1 can be written as (Housner 1963; Aslam et al. 1980):

$$\ddot{\theta} - p^2\theta = -p^2\alpha \tag{2}$$

in which $p = \sqrt{WR/I_0} = \sqrt{3g/(4R)}$.

Under more realistic conditions, energy dissipates during each impact of the block on the base. For inelastic impact (no bouncing), the reduction of kinetic energy r, depends on the square of the ratio of angular velocities $\dot{\theta}_i$ before and $\dot{\theta}_{i+1}$ after an impact, respectively (Housner 1963; Aslam et al. 1980; Augusti and Sinopoli 1992):

$$r = \left(\frac{1}{2} I_0 \dot{\theta}_{i+1}^2\right) / \left(\frac{1}{2} I_0 \dot{\theta}_i^2\right) = \left(\frac{\dot{\theta}_{i+1}}{\dot{\theta}_i}\right)^2 \tag{3}$$

and for slender blocks the coefficient of restitution is:

$$\eta = \sqrt{r} = \frac{2 - b^2/h^2}{2(1 + b^2/h^2)} = 1 - \frac{2}{3}\alpha^2 \tag{4}$$

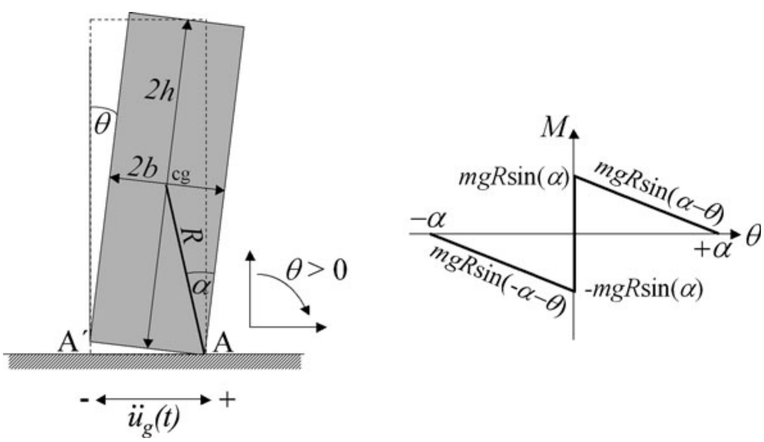

Fig. 4 Nomenclature for describing the rocking motion of a vertically oriented rectangular block. A and A' are the corner points of the block about which the block rocks; cg indicates the center of gravity, α is a measure of the slenderness of the block, and θ is the angle of inclination. The lateral acceleration of the ground is denoted $\ddot{u}_g$. The sketch on the right side shows schematically the restoring gravity moment M versus the rotation angle θ (after Housner 1963 and Augusti and Sinopoli 1992)

Housner (1963) showed that in this case the amplitude θ_n of the nth cycle can be written as:

$$\theta_n = 1 - \sqrt{1 - r^n\left[1 - (1 - \theta_0/\alpha)^2\right]} \qquad (5)$$

and the half period of the rocking motion is:

$$\frac{T}{2} = 2\sqrt{\frac{I_0}{WR}}\tanh^{-1}\sqrt{r^n\left[1 - (1 - \theta_0/\alpha)^2\right]} \qquad (6)$$

Amplitudes and the half period of the rocking motion decay rapidly with the number of cycles. Increasingly high-frequency movements follow a few slow rocking motions with large amplitudes. Under less ideal conditions, (bouncing during impacts and sliding due to reduced friction) amplitude decay proceeds even more rapidly.

Figures 5 and 6 show the acceleration time histories measured on the top of the free-rocking block with the sliding table in a fixed position for rocking along the short and long base line of the marble block, respectively. The starting position in both cases was close to the turnover point. In the first case (rocking parallel to the short 6 cm axis), the motion lasts about 6 s and in the second case about 4 s. When the block passes the equilibrium position the impact on the base plate causes a sharp impulse with high acceleration level in the vertical direction. The component labeled parallel is the one parallel to the rocking direction. The boxcar-like accelerogram with the decreasing width of the boxes and the concave bent top and bottom of the boxes result from the rocking motion itself. At the equilibrium position, the moment of impact, the sign of acceleration switches. The curvature of the accelerogram indicates the circle on which the accelerometer is moving during the rocking motion. Arrows indicate the theoretical times for the first ten impacts following Eq. 6 from Housner's (1963) model. Imperfections in the analog model, i.e., no absolute flat base, slightly rounded edges, cause an increasing deviation with time for the further impacts. The two horizontal acceleration components were bandpass-filtered between 0.8 and 50 Hz and integrated twice. The resulting pseudo-displacements were used to construct the hodograms shown in Figs. 5 and 6. The linear polarization indicates a pure rocking motion.

Subsequently numerous experiments were made during which the free-rocking motion was started as described above. However, after the first or second impact of the block, an impulsive motion of the sliding table was induced manually in the transverse

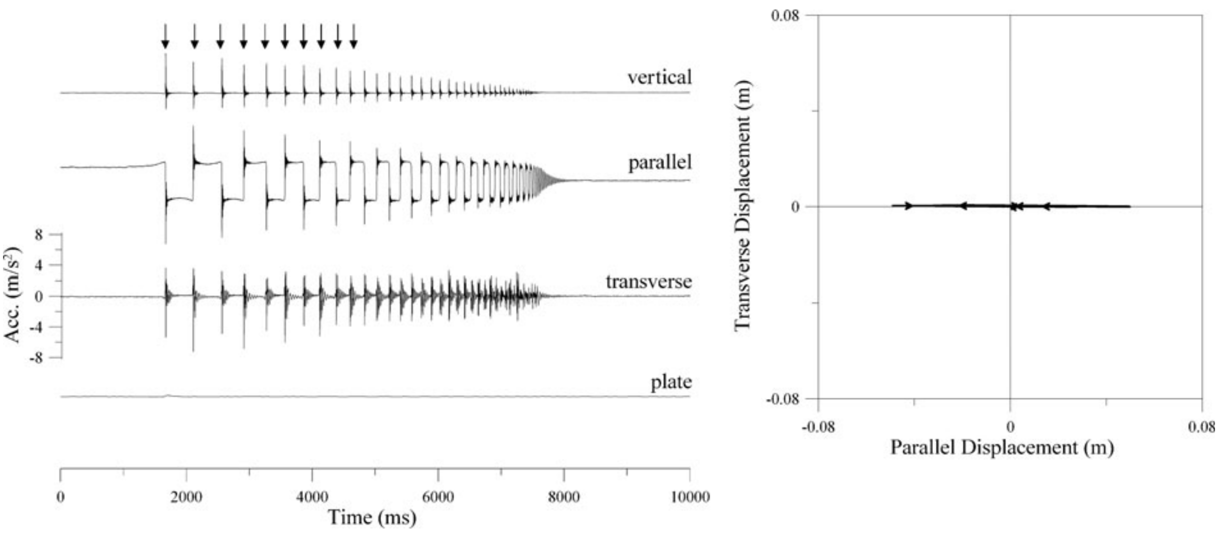

Fig. 5 Acceleration time histories (*left*) and displacement hodogram (*right*) of a free-rocking experiment with the marble block shown in Fig. 3. Rocking motion was parallel to the short (6 cm) axis. The top three traces are the acceleration measured on top of the marble block in vertical direction and parallel and transverse to the rocking motion, respectively. The vertical trace was scaled down by a factor of four with respect to the other traces. The bottom trace is the bandpass (0.8–10 Hz) filtered acceleration of the sliding table in transverse direction. The horizontal components of the marble block acceleration were bandpass-filtered (0.8–50 Hz) and integrated twice for the hodogram. *Arrows* above the top trace indicate the theoretical times of the first 10 impacts of the rocking block following the model given by Housner (1963)

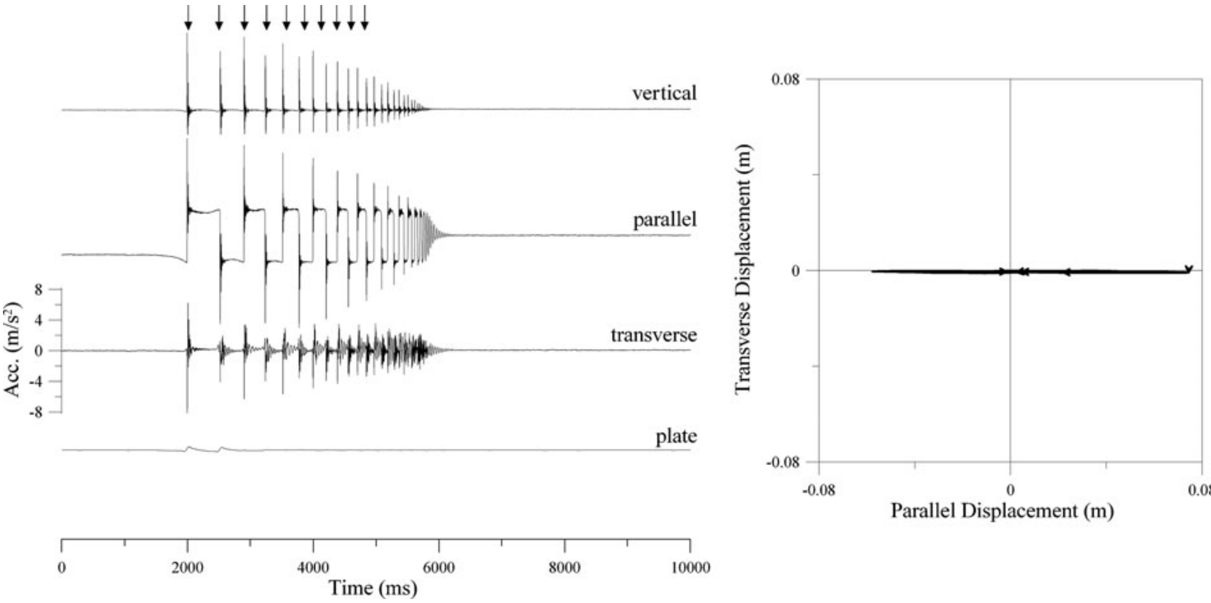

Fig. 6 Same as Fig. 5 for a free-rocking motion of the block parallel to the long (8 cm) axis of the marble block

direction, causing precession and rotations of the marble block. Depending on the exact moment and amplitude of this impulse, final rotations of the block of up to 40° were measured. cw and ccw rotations occurred roughly equally in the tests. Figure 7 shows an example of a free-rocking test parallel to the 6 cm axis with an impulsive disturbance in the orthogonal direction. The maximum acceleration of the sliding table is 5.4 m/s^2. Compared to the undisturbed experiment, the total duration of motion is significantly reduced; the final rotation of the block measures 30° cw. An example of a corresponding

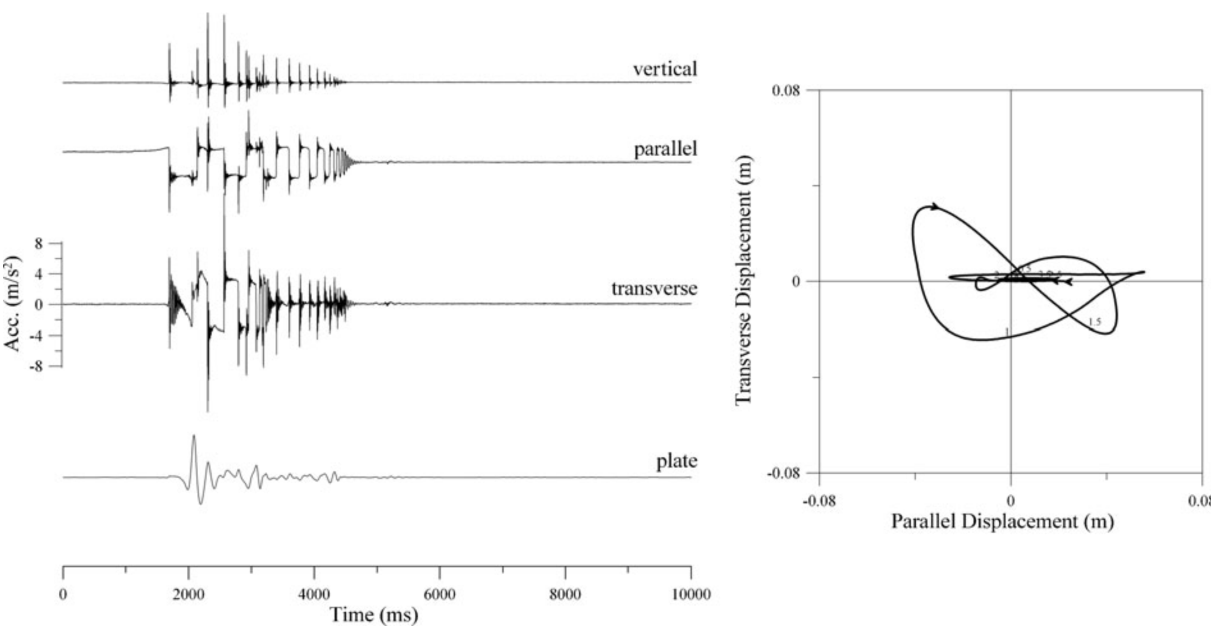

Fig. 7 Acceleration time histories and displacement hodogram of the marble block rocking parallel to the short (6 cm) axis. After the first impact of the block, an impulse in transverse direction shown in the bottom trace disturbed the free rocking. The numbers along the hodograms indicate time in seconds. The block rotated 30° in a clockwise direction

test with the rocking parallel to the 8 cm axis is given in Fig. 8. Here the maximum sliding table acceleration is 2.5 m/s^2, the reduction of total duration is smaller than in the previous example, and final rotation of the block is 26° ccw.

The hodograms of the free-rocking tests (Figs. 7 and 8) show that the movement is only about the rotation axis (transverse direction) when no disturbance occurs. The construction of the table guaranties a sliding motion only in the transverse direction. When such a motion occurs at the "right" moment, significant rotation may occur and reducing the amplitude of the rocking parallel component motion of the block. So once a rocking motion is initiated, ground motion in the orthogonal direction can induce rotation as suggested by, i.e., Hoffmann (1838), Mallet (1862), Reid (1910), and Yegian et al. (1994) ergo Kozák's (2009) Rot2 model.

In order to start a forced rocking motion sufficient friction between the block and the base and a horizontal acceleration a is necessary that fulfills the condition (Housner 1963; Augusti and Sinopoli 1992):

$$\frac{a}{g} \geq \frac{b}{h}. \tag{7}$$

An exceedance of this acceleration level in both horizontal directions might be a criterion for initiating a rotation about the vertical axis.

3 Numeric model

The numeric models in this study were realized with the program Universal Mechanism (Pogorelov 1995, 1997). The method assumes no deformable 3D objects as described by Kraus et al. (1997). After defining the physical parameters of the bodies, the type and degrees of freedom of the joints between blocks and the type and parameters of the contact forces, the code generates the equations of motion of the mechanical system. An implicit second-order method with variable step size is used to solve the equations of motion and the tolerance for the relative error of the calculated coordinate values was set to 10^{-6}. Typical average step size in the calculations is on the order of 10^{-4} s. The contact frequency (square root of stiffness divided by mass) was set to 200 Hz, an order of magnitude larger than the maximum frequency of the seismic data, and damping ratio of the coupling was 0.3. The density of all model blocks was set to 2.7 Mg/m^3, and the coefficients of static and dynamic friction to 0.7 and 0.6, respectively.

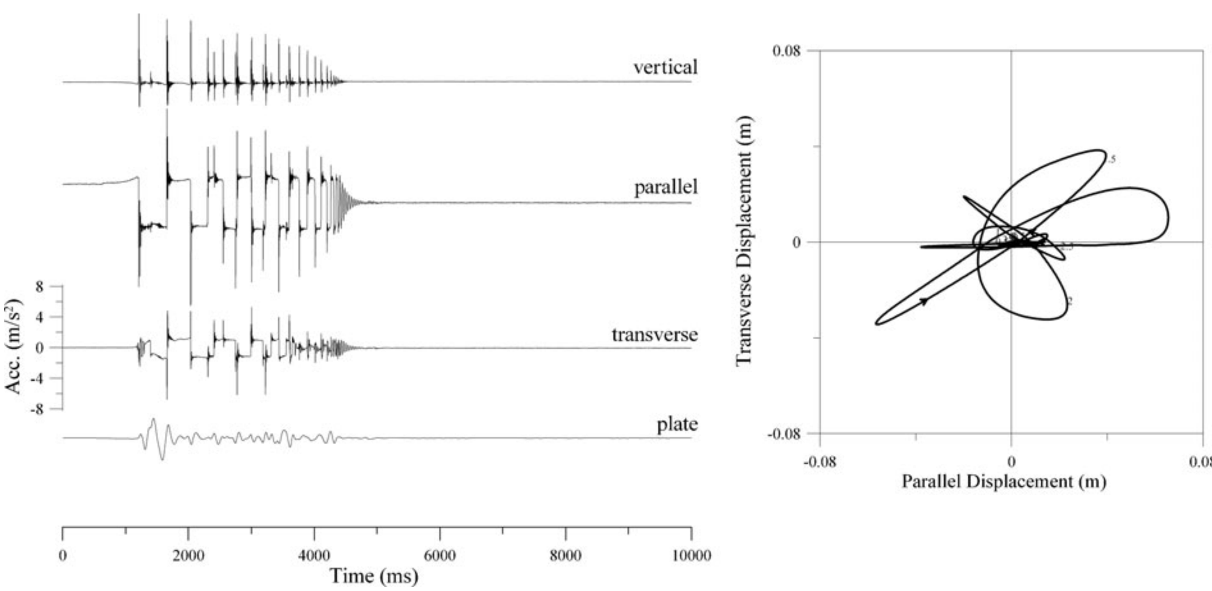

Fig. 8 Acceleration time histories and displacement hodogram of the marble block rocking parallel to the short (8 cm) axis. After the first impact of the block, an impulse in transverse direction shown in the bottom trace disturbed the free rocking. The numbers along the hodograms indicate time in seconds. The block rotated 26° in a clockwise direction

Verification tests of similar models, in which analytically solved problems of block rocking motions are compared with calculation results, are given by Hinzen (2009) and Hinzen (2011). The notations and conventions suggested by Evans (2009) for rotational seismology are used in the following.

3.1 Analytic ground motion signals

A simple cuboid with a square base of 0.5 m and a height of 3.0 m was used in a series of numeric experiments resembling the previously described analog tests in a more systematic way and with a block reaching the size of a monument. As an initial condition, the block was inclined to 0.1 rad, 60% of the critical angle of 0.167 rad. This initial condition introduces a free-rocking motion of the block about the X-axis. A one-sine acceleration ground motion pulse (cycloidal pulse) was applied to the base block during the rocking motion in the direction orthogonal to the rocking motion (Fig. 9). Amplitude A_{max} of the cycloidal pulse and its starting time t_0, defined as the delay time after the start of the free-rocking motion, were systematically varied. The rationale for the procedure was to test whether the susceptibility of the rocking block to rotation depends on the phase relation between the ongoing rocking motion and the orthogonal disturbance. The one-sine pulse can be written as:

$$\ddot{u}_g(t) = \begin{cases} A_{\max}\sin(\omega t + \varphi) & -\varphi/\omega \le t \le (2\pi - \varphi)/\omega \\ 0 & \text{else} \end{cases}, \tag{8}$$

where φ is the phase angle, and ω the angular frequency. In order to start a rocking motion of a resting block following Eq. 7 the acceleration level $u_g = \alpha g$ has to be reached or exceeded (i.e., Anooshehpoor et al. 2000; Zhang and Makris 2001; Hinzen 2011).

Results of a set of 961 experiments, in which the parameter space of A_{max} and t_0 were varied between 0.5 to 5.0 m/s^2 and 0.0 to 5.0 s, respectively, are shown in Fig. 10. The frequency of the impulse was 2.0 Hz. The state of the free-rocking motion of the block, when A_{max}=0 is shown for reference in the top of Fig. 10 in form of the rotation angle Φ_X. No rotation about the vertical axis occurs when the acceleration stays below the threshold needed to start rocking of a resting block; in this case, $u_g = 1.635\,\mathrm{m/s^2}$. When

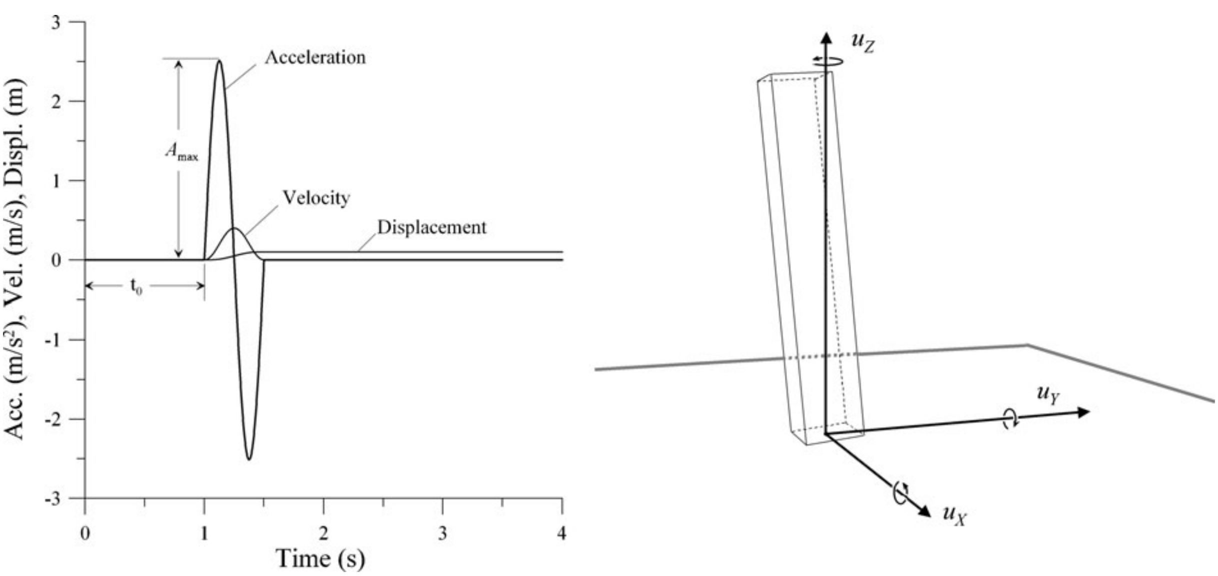

Fig. 9 *Left* cycloidal pulse used as a ground motion signal in numeric experiments with the discrete element model. Displacement, velocity, and acceleration of the pulse are shown. A_{max} is the maximum acceleration amplitude and t_0 a delay time measured from the beginning of the experiments to the first break of the impulse motion. *Right* orientation of the free-rocking block. The initial inclination is positive about the X-axis; the first (positive) amplitude of the cycloidal pulse is applied in the positive X-direction

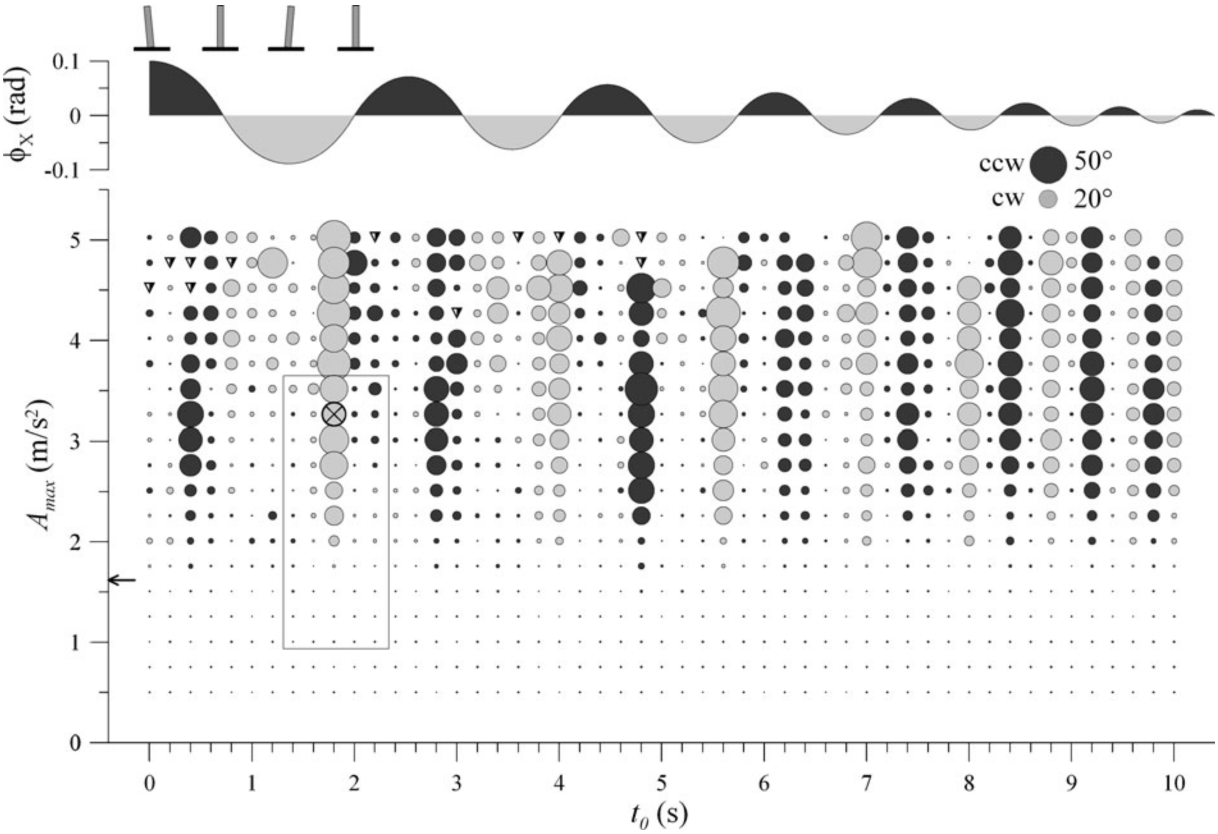

Fig. 10 Results of 969 numeric experiments in which a block of 0.5×0.5×3.0 m was subject to a free-rocking motion. The top trace shows the rotation angle about the *X*-axis of the block versus time; the *block symbols* indicate the amount and direction of inclination. Cycloidal pulses of ground motion with varying amplitude ($A_{\max}$) and start time t_0 were applied during the free-rocking motion. The pulses had a duration of 0.5 s (2.0 Hz). *Bubble size and shading* indicates the amount and sense of final rotation with respect to the vertical *Z*-axis at the end of the experiment (20 s). *Light- and dark-filled bubbles* indicate clockwise (*cw*) and counter-clockwise (*ccw*) rotation, respectively. *Triangles* show tests where the block toppled. The *arrow pointing to the abscissa* indicates the $A_{\max}$ threshold needed to start a rocking motion of the block from a resting position. The *rectangle* in the bottom plot marks a parameter range shown in Fig. 11 with a higher resolution, and the *crossed circle marks* the parameter combination for which the rotation–time history is shown in Fig. 12

the impulse acceleration exceeds this threshold, rotation is induced. Figure 10 shows that the amount of rotation and the sense of the rotation, cw and ccw, respectively, depend clearly on the phase relation between the ongoing free-rocking motion and the delay time t_0. The most susceptible times for initiation of rotation about the vertical axis are when the impulse starts as the block is approaching the equilibrium position, not as intuition would suggest, when it encounters the maximum inclination. The sense of rotation is determined by the stage of the free-rocking motion; when the block approaches equilibrium from a positive angle of inclination, the induced rotation is ccw. If the approach is from a negative angle of inclination, the rotation is cw as indicated by the bubble shadings in Fig. 10. With $A_{\max}$ exceeding 4 m/s^2, occasional toppling of the block occurs; however, this happens in a random pattern. Such a random component was also observed by Hinzen (2011), when testing the sensitivity of toppling columns to small changes in the initial conditions. The parameter range of the cycloidal pulse of $1.4 \le t_0 \le 2.2$ s and $1.0 \le A_{\max} \le 3.6$ m/s^2 is shown in Fig. 11 with a higher resolution. The U-shaped parameter range of significant ccw rotations of the block occurs before the impact of the block to the ground. Figure 12 shows the time history of the rotation angles for a cycloidal pulse with $t_0 = 1.8$ s and a PGA of 3.2 m/s^2; this parameter combination is marked in Fig. 10. In this case the rotation about the

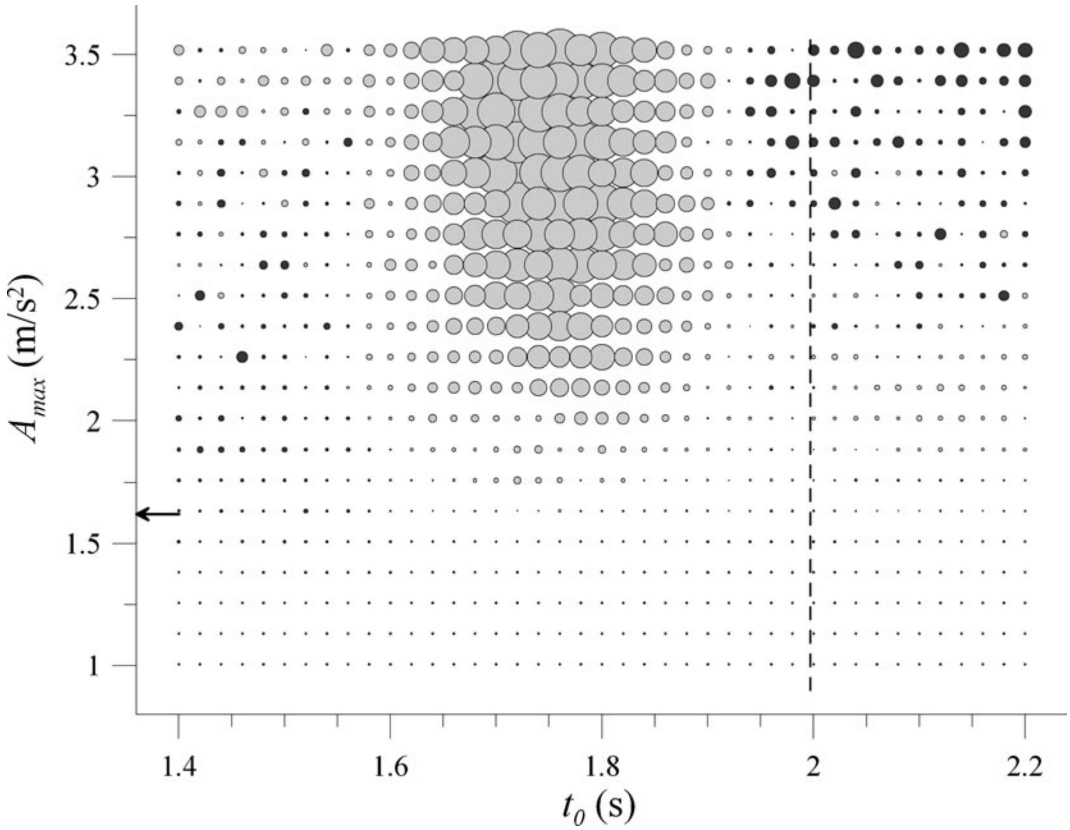

Fig. 11 Results of 861 numeric experiments for the parameter space of t_0 and $A_{\max}$ indicated in Fig. 10 by the rectangle. The *dashed line* indicates the time of the second impact of the block during its rocking motion about the *X*-axis. *Scaling and coloring of the bubbles* is the same as in Fig. 10

Z- and *Y*-axis starts immediately when the pulse reaches the threshold for the rocking initiation, increases within 3.8 s to its maximum, and reaches a final rotation angle of 45°.

An increase of the frequency of the cycloidal pulse to 4.0 Hz leads to smaller vertical rotations of the block (Fig. 13). Again, rotations occur only when the rocking threshold of acceleration is exceeded, and the inclination of the rocking block approaches the equilibrium position. However, the average of the vertical rotation for all tests with impulse accelerations above 1.6 m/s^2 is 4.4° compared to 12.7° in case of the 2 Hz impulses.

3.2 Recorded strong motion signals

We used two three-component strong ground motion acceleration records from the 2009 L'Aquila earthquake in Central Italy to study the rotational behavior of two models. Station AQV is located on soft rock and experienced the largest measured PGA (6.46 m/^{2}) during the earthquake; bedrock station AQG shows a PGA of 5.07 m/s^2. The first model is the cuboid from the previous section; in the second model, the cuboid was cut into two equally high blocks. These blocks initially rest on top of each other with no connection forces other than gravity.

The measured acceleration signals were integrated twice with respect to time to get translational ground motion displacements in three orthogonal directions. Figure 14 shows the results for the accelerograms from station AQV and the rotations of the model blocks. The rather harmonic looking rotations about the horizontal *X*- and *Y*-axes are reliable indicators for when a rocking motion is induced by the ground movement. This motion starts when the theoretical threshold of 1.635 m/s^2 is exceeded for the first time. For the single block model, a strong rotation about the *Z*-axis starts right away with the rocking motion. Within 1.9 s a cw rotation of 35° occurs; the

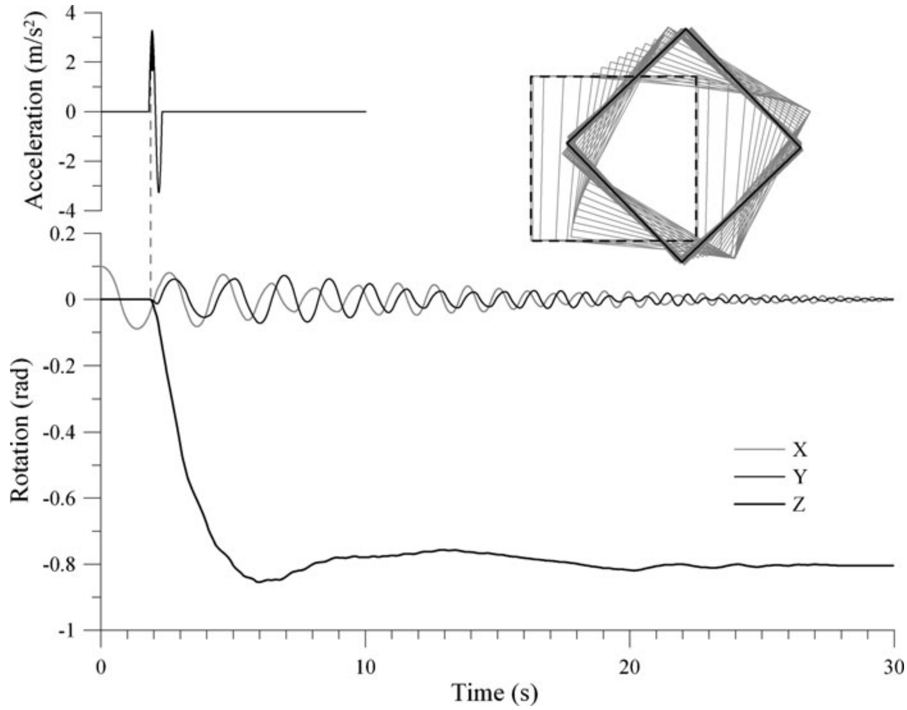

Fig. 12 Rotation–time history for a cycloidal pulse with t_0=1.8 s and PGA 3.2 m/s^2; the acceleration pulse itself is shown in the *left top of the figure*. In the *upper right part*, time snapshots of the position of the block's base are shown; the *dashed and continuous black lines* give the original and final position, respectively. Time increment for the gray position plots is 0.1 s. The *dashed line* indicates the time when the rocking threshold acceleration is reached by the cycloidal pulse

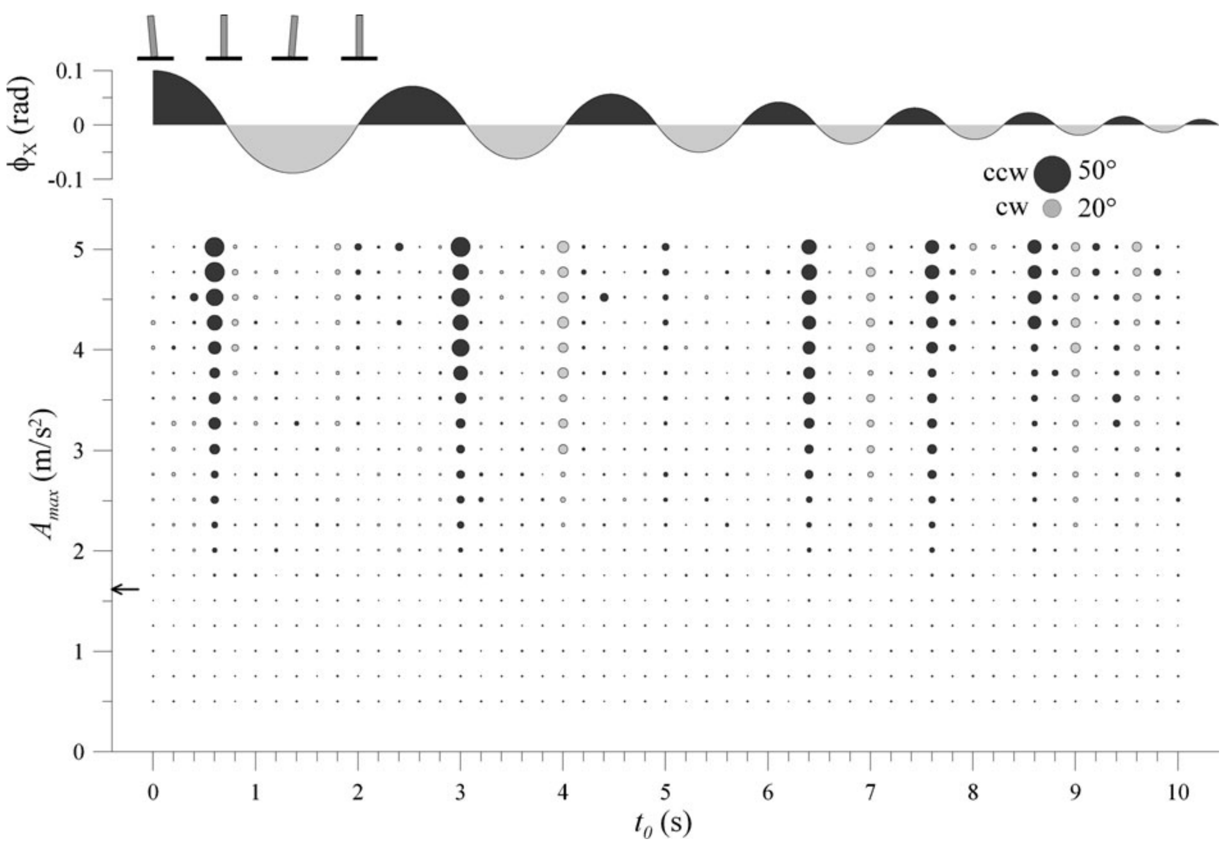

Fig. 13 Same as Fig. 10 for a cycloidal pulse with duration of 0.25 s (4.0 Hz)

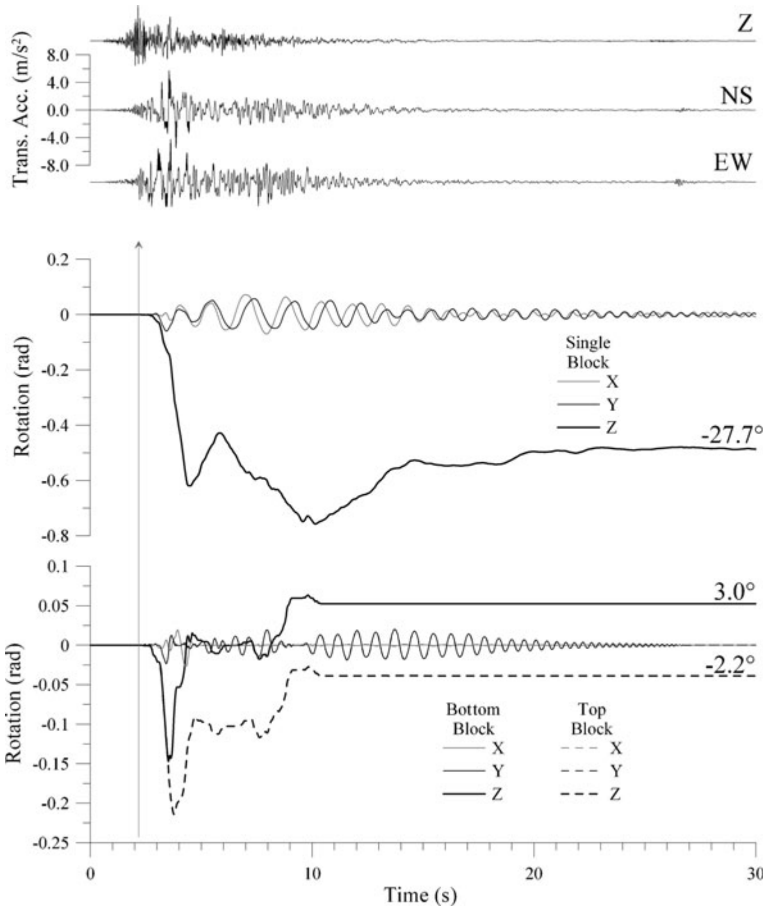

Fig. 14 Reaction of a 0.5×0.5×3.0 m vertically oriented cuboid to translational ground motion measured at station AQV during the 2009 L'Aquila earthquake. The top three traces show the acceleration in the vertical, north–south, and east–west directions, respectively; PGA (in the EW component) is 6.46 m/s^2. The *center diagram* shows the rotation angles about the three principal axes of the cuboid. The *bottom diagram* shows the rotations for two stacked blocks each with 1.5 m height. The *vertical arrow* indicates the moment when the minimum horizontal acceleration necessary for inducing a rocking motion is exceeded. The time windows during which this acceleration level is exceeded are indicated in the horizontal accelerograms by variable area traces. The *numbers at the ends of the curves* of vertical rotation give the final angle of rotation in degrees. Strong motion data are from Ameri et al. (2009)

maximum angle of rotation is 43° and the final rotation is 28°. In case of the double block model, the *X*- and *Y*-axes rotations are almost identical for the bottom and top block, respectively. The vertical rotations of both blocks are much smaller than in case of the single block model. The maximum values are 8° and 12° for the bottom and top block, both in cw direction; however, the final rotations are 3° ccw and 2° cw for the bottom and top block, respectively.

The results the AQG record (Fig. 15) show again a large final rotation of 31° cw is achieved for the single block model. In this case, the rotation about the *Y*-axis is significantly larger than about the *X*-axis. The same result is achieved using a double-block model. The bottom and top block rotate about the *Z*-axis in a similar way ending with final rotation values of 9° and 8°, both cw, for the bottom and top block, respectively.

4 Discussion and conclusion

Objects which rotate during earthquakes have long intrigued both laypersons and scientists. During the pre-instrumental period of seismology, the idea evolved to use rotations to deduce the location of

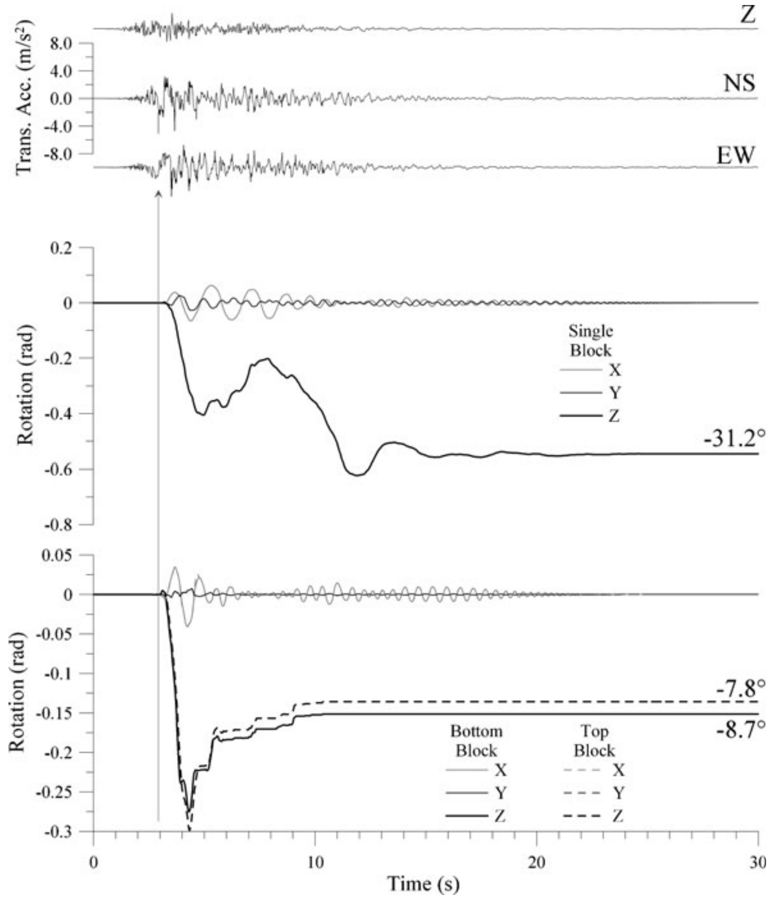

Fig. 15 Same as Fig. 14 for the 2009 L'Aquila earthquake record of station AQG; PGA (in the NS component) is 5.07 m/s^2. Strong motion data are from (Ameri et al 2009)

the earthquake source. These attempts were not successful, and with the advent of capable seismic instruments and location algorithms, rotation studies fell out of favor. Recent studies (Tertulliani and Maramai 1998) show that rotated simple objects might help constrain both the radiation pattern and source mechanism. This tool could help with quantifying such parameters for historic and prehistoric earthquakes. In the older studies on EROs (Fig. 2) the nature of the mapped objects is not always given in detail; however, many of these were vertically oriented objects, especially gravestones and monuments in cemeteries. Studies like that of Cucci and Tertulliani (2011) of EROs of the 2009 L'Aquila earthquake with detailed documentation of each ERO and subsurface conditions can be the basis for quantitative models that will help to learn more about the driving mechanisms.

While the location of earthquakes does not work based on EROs, these were used successfully to constrain ground motion amplitudes, especially when combined with observations of toppled objects. Simply structured objects worked best, such as those with a flat base resting on a flat foundation with no cementation or bolting. Frequently rotations of chimneys and other adobe structures are observed and documented in macroseismic studies. These structures are more complex in their dynamic behavior and harder to interpret in terms of rotation-causing ground motions. For example the motion of the whole building influences the rotation of chimneys. For simple analytic ground motions, the dynamic reactions of simple objects can be treated analytically (at least in 2D). For realistic earthquake ground motions in 3D, numeric models are necessary (Kamai and Hatzor 2008).

With analog and numeric models of vertically oriented objects, we have shown that pure translational ground motions in the horizontal plane are sufficient to induce vertical rotation. As shown in

Figs. 10 and 13, the phase difference between the inclination during an ongoing rocking motion around one horizontal axis and the ground motion parallel to this axis influences the amount and sense of a vertical rotation. The yield acceleration necessary to start rocking of a resting block is also a threshold for the initiation of the vertical rotation; however, the threshold has to be exceeded in both horizontal components. A similar interpretation was given by Yegian et al. (1994) and Athanasopoulos (1995) for monuments in graveyards in the Spitak area after the 1988 Armenian magnitude 7 earthquake. They concluded that rotations were caused by the twisting moment from the horizontal inertial force that acts on blocks while they are tilting in a rocking motion. This confirms the model called Rot2 by Kozák (2006). Reid (1910) called this “the principal of crost vibrations.” He assumed that the rotation lasts as long as the ground motion produces parallel rotation of the support. In the numeric tests of this study, a short cycloidal pulse in the direction parallel to the axis of an ongoing rocking motion was sufficient to start a vertical rotation lasting significantly longer than the impulse. The numerical experiments with analytic ground motions show that the phase relation of the two horizontal ground motion determines whether a rotation is cw or ccw. Due to the complexity of real strong ground motions, determined by the source process and local site conditions, and the additional vertical ground motion component under real earthquake conditions are strong arguments for rather random distributions of cw and ccw rotations of EROs as observed in most of the examples shown un Fig. 2.

These findings do not exclude the possibility that rotational ground motion components in the mesoseismal zone are also involved in the formation of EROs. With the improvement of direct rotational ground motion measurements (Bernauer et al. 2012) and the use of analytic approaches, where possible, and analog and numeric experiments, this problem will continue to be quantified in the future. This study with well-constrained conditions, ideal flat contact surfaces, evenly distributed contact forces, symmetric blocks with no eccentricity of the center of gravity, helps to define basic conditions for experiments with models of real objects. Several of the EROs described in the work of Cucci and Tertulliani (2011) have been surveyed with a laser scanner and model calculations are in progress.

Objects consisting of two or more stacked parts that exhibit differential rotations are of special interest for further studies. Specifically, if along the plane where the blocks connect, the dimensions exactly match differential rotations become interesting as the potential rocking points of the upper block coincide with the edges of the lower. Results of calculations using measured strong ground motions of the 2009 L’Aquila earthquake shown in Figs. 14 and 15 reveal that these 3D ground motions are capable of inducing significant rotations of up to 30° for a single block; however, significantly smaller rotations for stacked blocks of the same size as the single one. Such rotation angles meet the values observed at several objects during the L’Aquila and also during the recent Lorca earthquake in Spain. The abovementioned ongoing studies will give further insight to the mechanisms making objects rotate and will help to evaluate how much we can expect to learn about ground motions from EROs from historic and prehistoric times.

Acknowledgments I thank C. Fleischer for the help with the set up of the analog experiment and the institute’s workshop for building the sliding table. S. Dietz helped with the collection of the rotation data from literature and H. Kehmeier with editing the references. I am very thankful to S.K. Reamer for the stimulating discussions and the critical reading of the manuscript. The strong motion data of the L’Aquila earthquake were accessed through the Italian Accelerometric Archive at http://itaca.mi.ingv.it/ItacaNet/, last accessed December 2009. Two anonymous reviewers made very helpful suggestions which greatly improved the original manuscript during the review process.

References

Ameri G, Massa M, Bindi D, D’Alema E, Gorini A, Luzi L, Marzorati S, Pacor F, Paolucci R, Puglia R, Smerzini C (2009) The 6 April 2009 Mw 6.3 L’Aquila (Central Italy) earthquake: strong-motion observations. Seismol Res Lett 80:951–966

Anooshehpoor A, Heaton TH, Shi B, Brune JN (1999) Estimates of the ground accelerations at Point Reyes Station during the 1906 San Francisco earthquake. Bull Seismol Soc Am 89:845–853

Anooshehpoor A, Heaton TH, Shi B, Brune JN (2000) Reply to comment by J. Zhang and N. Makris on “Estimates of the ground accelerations at Point Rayes station during the 1906 San Francisco earthquake” by A. Anooshehpoor, T. H. Heaton, B. Shi, and J.N. Brune. Bull Seismol Soc Am 90:1349–1351

Aslam M, Godden WG, Scalise DT (1980) Earthquake rocking response of rigid blocks. J Struct Div 106:377–392

Athanasopoulos GA (1995) Discussion of "1988 Armenia earthquake. II: Damage statistics versus geologic and soil profiles". J Geotech Eng 121:395

Augusti G, Sinopoli A (1992) Modeling the dynamics of large block structures. Meccanica 27:195–211

Bernauer F, Wassermann J, Igel H (2012) Rotational sensors—a comparison of different sensor types. J Seismol, in press.

Brokesova J, Malek J, Kolinsky P (2012) Mechanical seismic sensor system for field rotation rate measurements and in-situ calibration. J Seismol, in press.

Cancani A (1903) Sur l'emploi d'une double échelle sismique des intensités, empirique et absolute. Verh. II Intern. Seismil.-Konf. zu Straßburg.

Cowsik R, Madziwa-Nussinov T, Wagoner K, Wiens D, Wysession M (2009) Performance characteristics of a rotational seismometer for near-field and engineering applications. Bull Seismol Soc Am 99:1181–1189

Cucci L, Tertulliani A (2011) Clues for a relation between rotational effects induced by the 2009 Mw 6.3 L'Aquila (Central Italy) earthquake and site and source effects. Bull Seismol Soc Am 101:1109–1120

Evans JR (2009) Suggested notation conventions for rotational seismology. Bull Seismol Soc Am 99:1073–1075

Frepoli A, Amato A (1997) Contemporaneous extension and compression in the Northern Apennines from earthquake fault plane solutions. Geophys J Int 129:368–388

Gordon DW, Bennett TJ, Herrmann RB, Rogers AM (1970) The south-central Illinois earthquake of November 9, 1968: macroseismic studies. Bull Seismol Soc Am 60:953–971

Grazier V, Kalkan E (2012) Large rotations extracted from strong motion records. J Seismol, in press.

Grünthal G (1993) European macroseismic scale 1992. Centre Européen de Géodynamique et de Séismologie, Luxembourg, pp. 79.

Gutenberg B (1927) Grundlagen der Erdbebenkunde. Gebrüder Bornträger, Berlin

Hinzen K-G (2009) Simulation of toppling columns in archaeoseismology. Bull Seismol Soc Am 99:2855–2875

Hinzen K-G (2010) Back calculation of earthquake rotated objects (EROs), 2nd Proceedings International Workshop on Rotational Seismology and Engineering Applications, Prague, 37.

Hinzen K-G (2011) Sensitivity of earthquake toppled columns to small changes in ground motion and geometry. Isr J Earth Sci (in press)

Hodgson EA (1950) The Saint Lawrence earthquake March 1, 1925. Publ Dom Observ Ottawa 7:363–436

Hoffmann F (1838) Zweiter Band: Geschichte der Geognosie und Schilderungen der vulkanischen Erscheinungen. Vorlesungen gehalten an der Universitaet zu Berlin in den Jahren 1834 und 1835. Nicolaische Buchhandlung, Berlin, pp. 596.

Housner GW (1963) The behavior of inverted pendulum structures during earthquakes. Bull Seismol Soc Am 53:403–417

Kamai R, Hatzor YH (2008) Numerical analysis of block stone displacements in ancient masonry structures; a new method to estimate historic ground motions. Int J Numer Anal Meth Geomech 32:1321–1340

Kirkpatrick P (1927) Seismic measurements by the overthrow of columns. Bull Seismol Soc Am 17:95–109

Kovach RL (2004) Early earthquakes of the Americas. Cambridge University Press, Cambridge, p 269

Kozák JT (2006) Development of earthquake rotational effect study. In: Teisseyre R, Takeo RM, Majewski E (eds) Earthquake source asymmetry, structural media and rotation effects. Springer, Berlin, pp 3–10

Kozák JT (2009) Tutorial on earthquake rotational effects: historical examples. Bull Seismol Soc Am 99:998–1010

Kraus PR, Fredriksson A, Kumar V (1997) Modeling of frictional contacts for dynamic simulation. IROS 1997 Workshop on Dynamic Simulation: Methods and Applications, Sept. 1997.

Lander AF (1968) Seismological notes January and February, 1968. Bull Seismol Soc Am 58:1705–1714

Makris N, Roussos YS (2000) Rocking response of rigid blocks under near-source ground motions. Géotechnique 50:243–262

Mallet R (1848) Dynamics of earthquakes. Trans R Irish Acad 21:50–106

Mallet R (1862) Great Neapolitanian earthquake of 1857, The First Principles of Observational Seismology, Vol. 2. Chapman and Hall, London, p 1600

Mauk FJ, Christensen D, Henry S (1982) The Sharpsburg, Kentucky, earthquake 27 July 1980: main shock parameters and isoseismal maps. Bull Seismol Soc Am 72:221–236

Nigbor RL, Evans JR, Hutt C (2009) Laboratory and field testing of commercial rotational seismometers. Bull Seismol Soc Am 99:1215–1227

Oldham RD (1899) Report of the great earthquake of 12th June, 1897. University of Michigan, Michigan, USA, reprint, pp. 560.

Pogorelov DY (1995) Numerical modelling of the motion of systems of solids. Comput Math Math Phys 35:501–506

Pogorelov DY (1997) Some developments in computational techniques in modeling advanced mechanical systems. In: van Campen DH (ed), Interaction between dynamics and control in advanced mechanical systems, Proc. IUTAM Symp. Eindhoven, The Netherlands, April 21–26 1996, pp. 313–320.

Reid HF (1910) The mechanics of the earthquake, California Earthquake of April18, 1906. Carnegie Institute, Washington, p 192

Richter CF (1958) Elementary seismology. W.H. Freeman, San Francisco, p 768

Rouse JT, Priddy RR (1938) Recent earthquakes in Western Ohio. Ohio J Sci 38:25–36

Schreiber KU, Hautmann JN, Velikoseltsev A, Wassermann J, Igel H, Otero J, Vernon F, Wells J-PR (2009a) Ring laser measurements of ground rotations for seismology. Bull Seismol Soc Am 99:1190–1198

Schreiber KU, Velikoseltsev A, Carr AJ, Franco-Anaya R (2009b) The application of fiber optic gyroscopes for the measurement of rotations in structural engineering. Bull Seismol Soc Am 99:1207–1214

Shi BP, Anooshehpoor R, Zeng YH, Brune JN (1996) Rocking and overturning of precariously balanced rocks by earthquakes. Bull Seismol Soc Am 86:1364–1371

Sieberg A (1923) Geologische, physikalische und angewandte Erdbebenkunde. Verlag von Gustav Fischer, Jena, pp. 572.

Stupazzini M, de la Puente J, Smerzini C, Käser M, Igel H, Castellani A (2009) Study of rotational ground motion in the near-field region. Bull Seismol Soc Am 99:1271–1286

Takamori A, Araya A, Otake Y, Ishidoshiro K, Ando M (2009) Research and development status of a new rotational seismometer based on the flux pinning effect of a superconductor. Bull Seismol Soc Am 99:1174–1180

Tertulliani A, Maramai A (1998) Macroseismic evidence and site effects for the Lunigiana (Italy) 1995 Earthquake. J Seismol 2:209–222

Trifunac MD (2009) The role of strong motion rotations in the response of structures near earthquake faults. Soil Dynam Earthquake Eng 29:382–393

Ulrich FP (1936) Helena earthquakes. Bull Seismol Soc Am 26:323–339

Whittington ML, Pascek S (2005) Magnitude 6.7 Charlevoix-Kamouraska eartquake of February 28, 1925 (St. Lawrence, Canada), St. Louis University, http://www.eas.slu.edu/eqc/eqc_photos/1925EQ/. Accessed 3 October 2011.

Wood HO, Neumann F (1931) Modified Mercalli intensity scale of 1931. Bull Seismol Soc Am 21:277–283

Yamaguchi R, Odaka T (1974) Field study of the Izu-Hantooki earthquake of 1974. Special Bulletin of the Earthquake Research Institute, Tokyo 14:241–255

Yang F, Luo Q, Che W (2010) Torsional phenomena in 2008 great Wenchuan earthquake. Earthquake Science 23:79–85

Yegian MK, Ghahraman VG, Gazetas G (1994) 1988 Armenia Earthquake. II: Damage statistics versus geologic and soil profiles. Journal of Geotechnical and Geoenvironmental Engineering 120:25

Zhang J, Makris N (2000) Comment on “Estimates of the ground accelerations at Point Rayes station during the 1906 San Francisco earthquake” by A. Anooshehpoor, T. H. Heaton, B. Shi, and J.N. Brune. Bull Seismol Soc Am 90:1342–1348

Zhang J, Makris N (2001) Rocking response of free-standing blocks under cycloidal pulses. J Eng Mech 127:473–783